Nano Research 2017, 10(1): 320–330
DOI 10.1007/s12274-016-1294-4
Research Article
ISSN 1998-0124
CN 11-5974/O4

Embedding variable micro-capacitors in polydimethylsiloxane for enhancing output power of triboelectric nanogenerator

Xiaona Xia[1], Jie Chen[1], Hengyu Guo[1], Guanlin Liu[1], Dapeng Wei[2], Yi Xi[1], Xue Wang[1] (✉), and Chenguo Hu[1] (✉)

[1] *Department of Applied Physics, Chongqing University, Chongqing 400044, China*
[2] *Chongqing Key Laboratory of Multi-scale Manufacturing Technology, Chongqing Institute of Green and Intelligent Technology, Chinese Academy of Sciences, Chongqing 400714, China*

Received: 2 August 2016
Revised: 13 September 2016
Accepted: 19 September 2016

KEYWORDS
cellular structure, polydimethylsiloxane, silver nanoparticles, variable micro-capacitor

ABSTRACT

Polydimethylsiloxane (PDMS) is an excellent material for investigating the mechanism of triboelectricity as it can easily be used to construct various microstructures. In this study, micro-capacitors (MCs) and variable micro-capacitors (VMCs) were embedded in PDMS by filling PDMS with silver nanoparticles (NPs) and constructing an internal cellular structure. The output performance of the triboelectric nanogenerators (TENGs) based on MCs@PDMS and VMCs@PDMS films was systematically investigated, with variation of the filling content of silver NPs and the pore ratio and size. The microstructure, permittivity, dielectric loss, and capacitance of the VMCs@PDMS films were well characterized. The output current of the TENG based on the VMCs@PDMS film was respectively 4.0 and 1.6 times higher than that of the TENGs based on the pure PDMS film and MCs@PDMS film, and the output power density of the former reached 6 $W \cdot m^{-2}$. This study sheds light on the physical nature of conductive nanoparticle fillings and cellular structures in dielectric triboelectric polymers.

1 Introduction

Recently, a triboelectricity nanogenerator (TENG) for harvesting ambient environmental energy based on triboelectrification and electrostatic induction has attracted much attention [1–6], and various novel electrode structures have been designed to harvest wind [7–10], water-wave [11–16], sound [17, 18], and body movement energy [19], as well as other mechanical energy from the environment [20, 21]. Most studies on TENG devices focus on structural design to meet various environmental energy supply conditions [9, 11, 16, 22, 23] and to improve the output power through rational energy management [24, 25]. On the

Address correspondence to Xue Wang, xuewang@cqu.edu.cn; Chenguo Hu, hucg@cqu.edu.cn

other hand, some investigations have focused on modification of tribo-materials to enhance the energy conversion efficiency [26–32]. In those previous studies, modifications of tribo-materials have been carried out via two main approaches: (1) patterning the surface of electrodes and polymers [30, 31, 33] and (2) filling polymers with nanoparticles (NPs) or forming pores in polymers [26–29]. However, the physical nature of the nanoparticle fillers and porous structures of triboelectric materials are still not well understood.

In terms of materials chemistry, polydimethylsiloxane (PDMS) is a great material for investigation of the triboelectric mechanism as it can be easily used for constructing various microstructures inside another material. PDMS has excellent ability to trap negative charges. Previous work on modification of PDMS by filling with high permittivity NPs or conductive carbon NPs in PDMS [28, 29] and forming porous sponge-structures or porous sponge-structures with Au NPs [34] is limited, though these approaches can effectively enhance the electrical output. By analyzing the results of prior studies, we propose that maximizing the accumulation of tribo-charges on the surface of PDMS is in fact necessary for maximizing the capacitance of TENGs with the vertical contact-separation structure [35–38]. High permittivity NPs embedded in PDMS film were found to increase the relative dielectric constant of the polymer [28], whereas embedding carbon NPs in PDMS films reduced the effective thickness of the resulting films [29]. The porous sponge-structure of PDMS gives rise to a large specific area and good compressibility. These features increased the friction area and reduced the effective thickness of PDMS when it was pressed [34]. All of these results comply with our proposed "maximizing capacitance hypothesis" as they conform to the relation $C = \varepsilon S/d$. Therefore, exploration of new ways to enhance the capacitance of TENGs with the capacitor structure should be an effective strategy for improving the electrical output of such devices.

In this study, to enhance the capacitance of TENGs with the capacitor structure, we embed micro-capacitors (MCs) and variable micro-capacitors (VMCs) in PDMS by filling PDMS with silver NPs and constructing cellular structures in PDMS. The microstructure, relative permittivity, dielectric loss, and capacitance of the VMCs@PDMS films are evaluated by varying the filling content of the silver NPs and the ratios and sizes of the material pores. The output current of the TENG is effectively improved based on the VMCs@PDMS film, with an output power density of up to 6 $W \cdot m^{-2}$ at the resistance load of 20 MΩ. The developed device can be used to light about one hundred green light emitting diodes (LEDs) in series with good stability after thousands of recycles. A novel approach for utilizing conductive nanoparticle fillers and porous structures in PDMS is proposed herein.

2 Experimental

2.1 Fabrication of MCs@PDMS film

The MCs@PDMS film was prepared by filling silver NPs (Fig. S1(a) in the Electronic Supplementary Material (ESM)) in PDMS. Figure 1 shows the details of the fabrication process. In this experiment, the PDMS solution (Sylgard 184, Dow Corning) contained both the elastomer (PDMS) and the curing agent in a weight ratio of 10:1. First, the elastomer was placed in a culture dish, and the silver NPs were added in different proportions. To facilitate uniform dispersion of the particles in PDMS, the mixture was stirred quickly with a stick for half an hour. The curing agent was then added to the prepared mixture with stirring for another 10 min, and the mixture was subsequently transferred to a square acrylic template (hereafter, self-control pattern) and was kept at 330 K for 2.5 h to cure. Finally, the MCs@PDMS composite film was peeled off from the template.

2.2 Fabrication of VMCs@PDMS film

A VMCs@PDMS film was prepared by filling PDMS with silver NPs and constructing a cellular structure in PDMS. The same procedure mentioned above was implemented, except that in the second step, sugar particles with different sizes were mixed into the prepared mixture (of silver NPs and elastomer) in varying amounts (Fig. S1(b) in the ESM). To dissolve the sugar particles, the final composite film was placed into water at a temperature of 335 K under stirring

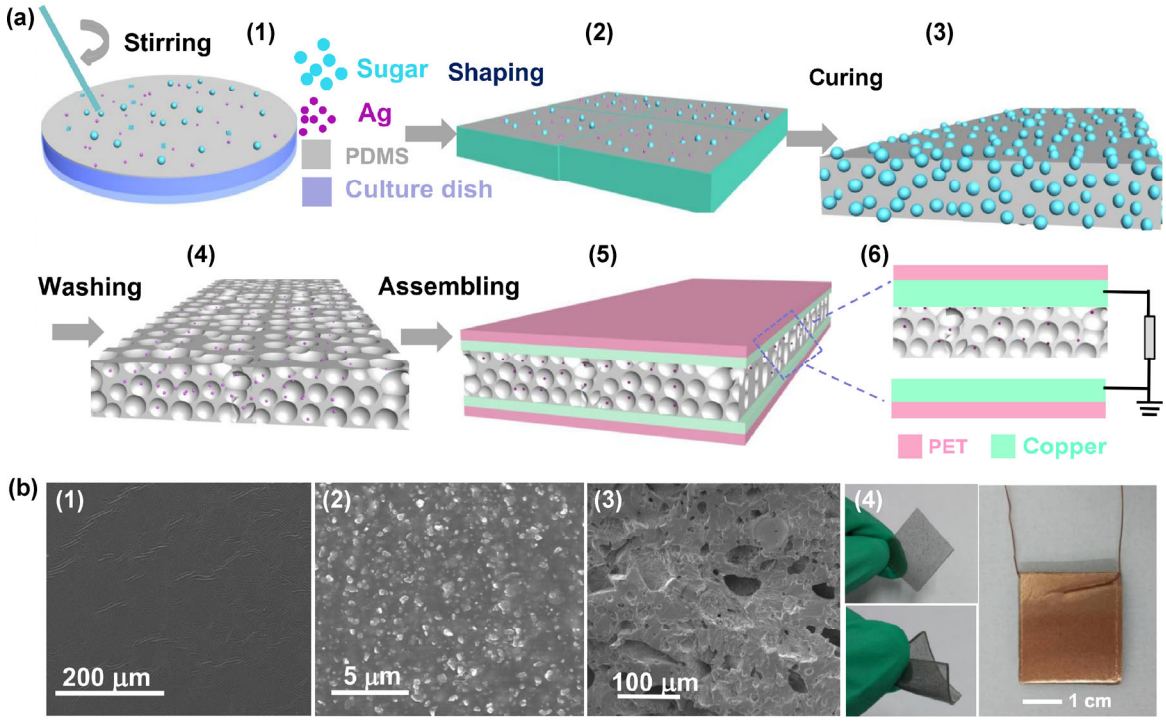

Figure 1 Schematic of process for fabricating the VMCs@PDMS thin film and TENG. (a) (1) Stirring the silver NPs and sugar particles uniformly in the culture dish, (2) shaping in the self-control pattern, (3) curing film at the temperature of 330 K in the oven and then peeling it off, (4) VMCs@PDMS composite film obtained by removing the sugar particles with water, (5) and (6) assembling with copper foil electrode and external circuit. (b) (1) SEM images of the pure PDMS film, (2) MCs@PDMS composite film, and (3) cross-section of the VMCs@PDMS film. (4) Digital image of flexible PDMS composite film and TENG.

for 76 h until the sugar particles were removed completely. Here, the washing process was very critical to ensure a completely clean and uniform VMCs@PDMS composite thin film. The porosity could be controlled by adjusting the amount of sugar particles added to PDMS. Finally, the composite film with silver NPs embedded in cellular PDMS was obtained after drying in an air-drying oven. The process is shown in Figs. 1(a)(1)–1(a)(4).

2.3 Fabrication of TENG based on VMCs@PDMS film

The TENG based on the VMCs@PDMS film had a sandwich structure arranged as: polyethylene terepthalate (PET, 50 μm) → copper foil (50 μm) → VMCs@PDMS film (800 μm) → copper foil → PET (from bottom to top), where the copper foils served as the electrodes and were connected to the copper wire and external load; the PET layers served as substrates. The device with dimensions of 2 cm × 2 cm × 2 mm had a certain gap between the bottom electrode and the surface of the VMCs@PDMS film, as shown in Figs. 1(a)(5) and 1(a)(6).

2.4 Characterization of TENG based on the VMCs@PDMS film

The morphology and structure of the VMCs@PDMS thin film were characterized by using a field emission scanning electron microscope (Nova 400 Nano SEM). X-ray diffraction analysis (XRD; Cu-Kα radiation; wavelength 1.5418 Å; 2 °·min^{-1} scanning speed) was used to study the crystal phase (Fig. S1(c) in the ESM). The line motor (WMU1536075-090-D) integrated with the device was employed to produce uniform pressure and control the displacement and frequency, and an optical microscope was also used to display the internal micropore structure of PDMS prepared with sugar particles of different sizes. The output performance of the TENG based on the VMCs@PDMS film was measured by using a Stanford low-noise current

preamplifier (Model SR570), a Keithley voltage preamplifier (Model 6514) and a Data Acquisition Card (NI PCI-6259) (NI PCI-6259).

3 Results and discussion

Figures 1(a)(1)–1(a)(4) illustrate the process for fabricating the VMCs@PDMS film and the TENG based on the film. The process comprises the following main steps: mixture stirring, shaping, curing, washing, and assembling. The detailed fabrication steps can be found in the Experimental section. As is shown in Fig. 1(a)(4), the sliver NPs may either be distributed in PDMS or localized in the holes. The SEM images of pure PDMS (Fig. 1(b)(1)) and the MCs@PDMS film (Fig. 1(b)(2)) indicate that the surface of the pure PDMS film was smooth, while some Ag nanoparticles could be seen on the surface of the MCs@PDMS film. In order to evaluate the internal structure in detail, a cross-sectional SEM image was acquired by cutting the VMCs@PDMS film vertically (Fig. 1(b)(3)). The image clearly shows well-formed holes in the VMCs@PDMS film, which is quite different from the case of the pure PDMS and MCs@PDMS films. The structure of various PDMS composite films is also shown in Fig. S2 (in the ESM). To investigate the influence of the micro-capacitors formed by addition of the Ag NPs to PDMS on the performance of the TENG based on the PDMS film, different amounts of sliver NPs (0 wt.%–4 wt.%) were added to PDMS. Figure 1(b)(4) displays the digital photograph of the MCs@PDMS composite thin film (Ag, 0.5 wt.%). The film was evidently smooth and semitransparent with good flexibility, and could be warped to any angle. The TENG was assembled using copper foil electrodes with the composite film in the middle; the TENG had dimensions of 2 cm × 2 cm × 2 mm (Fig. 1(b)(4)).

3.1 Influence of micro-capacitors formed in the PDMS film

To investigate the role of the micro-capacitors in improving the output performance of the TENG, different amounts of sliver NPs (0.00–0.04 g) were embedded into PDMS to form films. The output currents of the TENGs based on the different MCs@PDMS films were measured under an external periodic force at a frequency of 3 Hz; the output current increased from 8.18 μA (0.0 wt.% Ag) to 20 μA (0.5 wt.% Ag), as shown in Fig. 2(a). Further, the quantity of charge transferred (hereafter, transferred charge quantity) in one cycle increased with an increase of the Ag content to reach a maximum at 0.5 wt.% Ag (Fig. 2(b)). Both the output current and transferred charge quantity began to decrease when the Ag content exceeded 0.5 wt.%. It can be understood that the conductive Ag NPs form a large number of micro-capacitors in PDMS, which increases the capacitance of the TENG based on the MCs@PDMS film; therefore, the ability of the TENG to store charge is improved. The nonlinear current or transferred charge quantity curves might be caused by the agglomeration of superfluous Ag NPs in PDMS. In order to further analyze the capacitance change of the TENG, the capacitance of the MCs@PDMS composite films with different amounts of sliver NPs was measured, as shown in Fig. 2(c). The shape of the curve matched well with the results in Figs. 2(a) and 2(b), indicating that the maximum capacitance of the MCs@PDMS composite film was achieved with 0.5wt.% Ag. Digital photographs of the films with different Ag contents (0 wt.%–4 wt.%) are shown in Fig. 2(g), illustrating a reduction of the transparency of the MCs@PDMS film with an increase in the Ag content. The relative permittivity and dielectric loss of the MCs@PDMS films with different Ag contents were also measured, as summarized in Table S1 (in the ESM). Both the relative permittivity and the dielectric loss showed an evident increase with an increase of the Ag content of the film. Although higher permittivity can enhance the charge storage of the capacitor, higher leak electricity can reduce the charge storage. Therefore, based on a balance of these two properties, the maximum capacitance was achieved at a Ag loading of 0.5 wt.%. The corresponding current density and open-circuit voltage of the TENGs based on MCs@PDMS films with different Ag contents are shown in Fig. S3 (in the ESM).

3.2 Influence of cellular structure formed in PDMS film

In order to achieve variable micro-capacitors showing a response to pressure, a cellular structure was

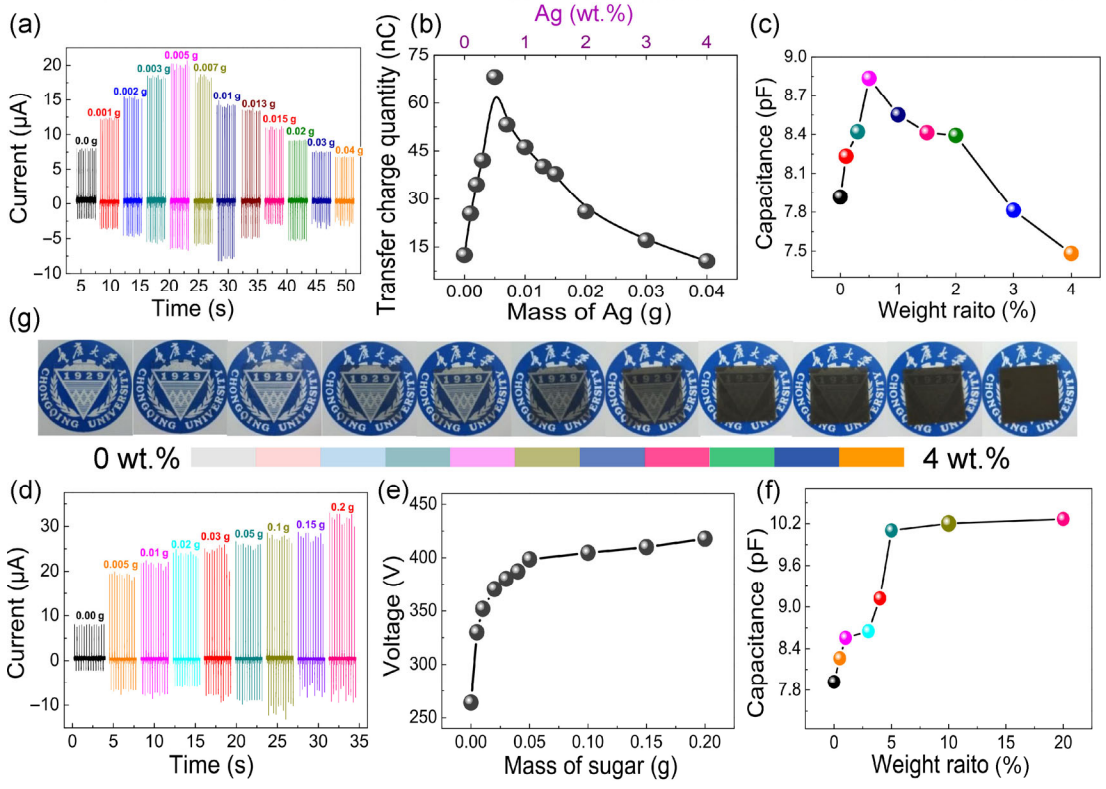

Figure 2 (a) Output short-circuit current, (b) transfer charge quantity, and (c) capacitance of TENG based on MCs@PDMS films, measured at a frequency of 3 Hz. (d) Output short-circuit current, (e) open-circuit voltage, and (f) capacitance of TENG with different VMCs@PDMS films. (g) Digital images of different PDMS films made by filling PDMS with different amounts of silver NPs.

conferred to the MCs@PDMS film by adding and removing sugar particles; the resulting film is denoted as VMCs@PDMS film. Because the peak output was obtained with the TENG based on PDMS with 0.5 wt.% Ag NPs, the VMCs@PDMS films were fabricated with different sugar weight ratios from 0–20% (hereafter, we indicate the sugar weight ratio to the porosity ratio for simplification) at a fixed Ag content of 0.005 g (0.5 wt.%). Figures 2(d) and 2(e) show the output current and voltage signals of the TENG based on the VMCs@PDMS film, from which it is evident that the output current and voltage were greatly enhanced with an increase in the porosity ratio from 0.0 to 0.5%; thereafter, the signals increased slowly. The output current is respectively nearly 1.6 and 4 times higher than that of the MCs@PDMS film and the pure PDMS film at the porosity ratio of 20%. The maximum voltage exceeded 400 V at the porosity ratio of 20% under the fixed periodic force at a frequency of 3 Hz. The corresponding current density plot is presented in Figs. S4(a) and S4(b) (in the ESM). The capacitance, relative permittivity, and dielectric loss of the VMCs@PDMS film are listed in Table S1 (in the ESM). The relative permittivity remained almost constant, while the capacitance and dielectric loss increased with an increase in the porosity ratio. It is easy to understand that the cellular structure formed in the PDMS film would reduce the thickness of the film and increase the surface area under external pressure, which increases the capacitance and leak current of the film. The detailed analysis of the capacitance from the variable micro-capacitors in PDMS is presented below.

On the other hand, the size of the pores in the VMCs@PDMS film might also influence the performance of the TENG. To obtain mesoporous VMCs@PDMS films with different pore sizes, 0.2 g (20 wt.%) of soluble sugar particles with sizes of about 80, 500, and 1,000 μm (Fig. S4(c)) was respectively mixed into PDMS solutions during the preparation process; 0.5 wt.% Ag NPs was

simultaneously mixed into the PDMS solution. The output current signals of the TENGs based on different VMCs@PDMS films with large, medium, and small pore sizes are plotted in Fig. 3(a). The output current decreased as the size of the cellules increased, but was higher than that of the flat PDMS film. The maximum value exceeded 30 μA at a porosity ratio of 20%, with pores of about 80 μm. This is because the denser cellular structure forms more variable micro-capacitors. In addition, the output current of the TENG based on the VMCs@PDMS film was 1.4 times higher than that of the TENG based on the MCs@PDMS film, which further proves the importance of variability for these micro-capacitors. The transferred charge quantity followed a trend similar to that of the output current, with the sizes of the pores and the highest transferred charge value being 96 nC in one cycle (Fig. 3(b)), indicating that a higher density of pores produces a larger charge transfer quantity. Photographs of the mesoporous VMCs@PDMS films fabricated with 20 wt.% of sugar particles having different sizes and with 0.5 wt.% Ag NPs are shown in Fig. 3(c), from which it is evident that pores with various dimensions were distributed in the PDMS film.

3.3 Other factors affecting TENG based on VMCs@PDMS film

As is well known, mechanical vibration in the ambient atmosphere is uncertain and alterable. To harvest mechanical energy from the environment, the influence of different driving frequencies on the TENG based on the VMCs@PDMS film was evaluated in the frequency range of 0.5 to 4 Hz. Figure 4(a) displays the dependence of the output current on different frequencies, illustrating that the output increases with an increase in the frequency. Faster contact and separation were achieved at a higher frequency, resulting in more transferred charge per second.

Furthermore, the output current was measured under application of different forces (F) to the TENG (Fig. 4(b)). The maximum output current of 23 μA was obtained at F_0, indicating that the output current increases with an applied force lower than F_0 and decreases when the force exceeds F_0. Because the area of contact between the mesoporous VMCs@PDMS film and the copper foil electrode increases and the effective thickness decreases with an increase of the applied force, the capacitance of the TENG increased,

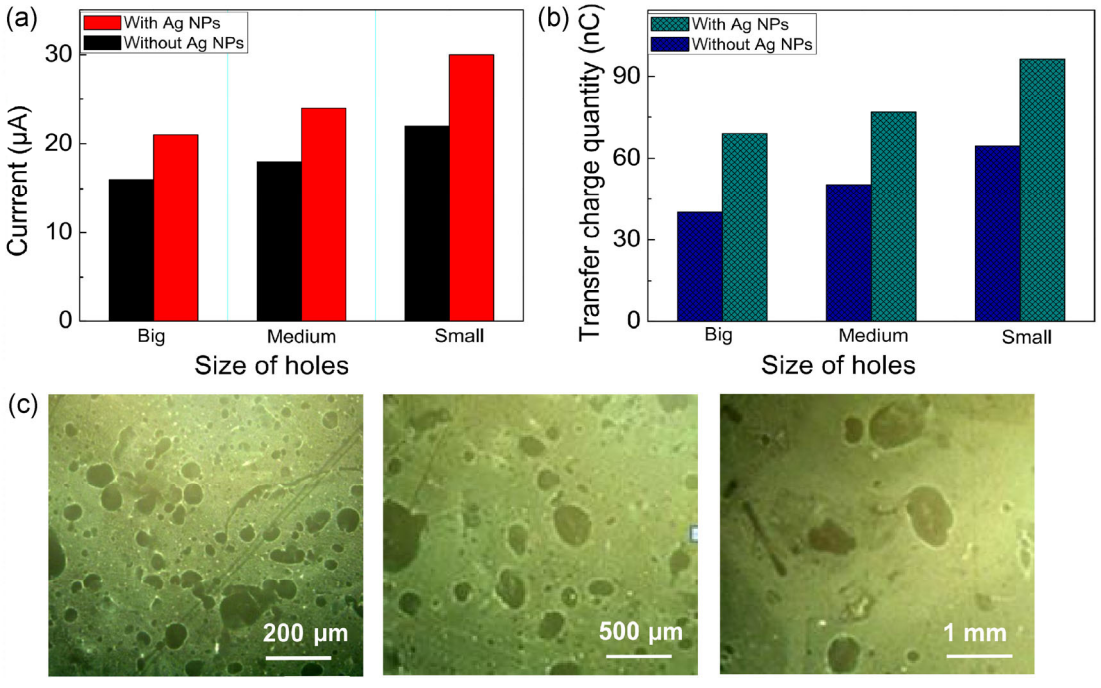

Figure 3 (a) Output current and (b) charge transfer quantity versus pore size of PDMS with silver NPs (red) and without silver NPs (black); (c) light microscope images of PDMS composite films with different pore sizes.

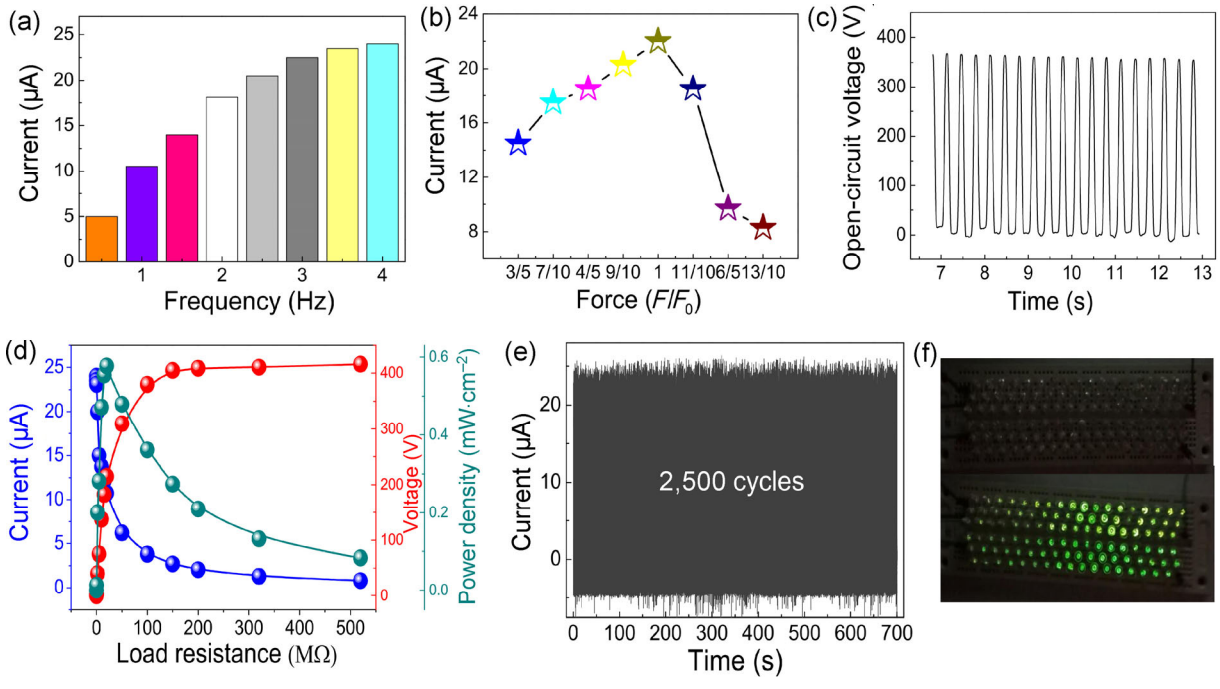

Figure 4 (a) Output current of TENG under different driving frequencies of f = 0.5, 1, 1.5, 2, 2.5, 3, 3.5, and 4 Hz, (b) effect of external pressure, (c) open-circuit voltage with 0.5 wt.% silver NPs and 5 wt.% sugar particles. (d) Maximum output voltage, current, and power density under different external loads, (e) stability/durability test of TENG for 2,500 cycles, (f) digital photographs of green LEDs lit by the TENG

resulting in an increase of the output current under a force less than F_0. However, too strong a force would induce chain formation by the Ag NPs in PDMS, which causes leak current. Therefore, the output current dropped when the applied force exceeded F_0. The open-circuit voltage for the TENG based on PDMS with 0.5 wt.% Ag NPs and having 5% porosity was measured under the applied force F_0, as shown in Fig. 4(c); the value reached 378 V. In addition, the output current, voltage, and power density were measured with application of different external load resistances from 110 KΩ to 520 MΩ. The maximum output power of 6 W·m^{-2} was achieved at the load of 20 MΩ, as shown in Fig. 4(d). The stability/durability of the device was demonstrated over 2,500 cycles (Fig. 4(e)), indicating good stability after long-term operation, and the device could be used to illuminate one hundred green LEDs in series (Fig. 4(f)). The output performance with variation of the relative humidity (RH) is summarized in Fig. S5 (in the ESM). The open-circuit voltage decreased with an increase of the RH; this response can be used to detect variation of the RH of the surroundings.

3.4 Working principle of TENG

The vertical contact mode generator acts both as an energy storage and output device. The maximum energy storage and output depend on the capacitance of the device [19].

For ideal parallel plate capacitors, the capacitance is described as follows

$$C = \varepsilon_0 \varepsilon_r S/d \tag{1}$$

where ε_0, ε_r, S, and d are the vacuum permittivity, relative permittivity, electrode surface, and thickness of the dielectric film, respectively. The maximum storage energy density is

$$\omega_{max} = \frac{1}{2}\varepsilon_0 \varepsilon_r E_{break}^2 \tag{2}$$

where E_{break} is the break down voltage, which depends on the dielectric properties of a dielectric material. The energy storage of the capacitor is described by

$$W = \frac{1}{2}CU^2 \tag{3}$$

where U is the voltage between two electrodes, which is directly related to the capacitance of the device.

Based on electromagnetism, when two pieces of metal plates with thickness r are inserted into a dielectric material, the capacitance increases as the whole capacitor can be regarded as three capacitors in series, as shown in Fig. 5(a), where the capacitance is

$$\frac{1}{C}=\frac{1}{C_i}+\frac{1}{C_i}+\frac{1}{C_i}, \quad C=\frac{\varepsilon_0\varepsilon_r S}{d-2r} \tag{4}$$

If we insert n pieces of the same metal plates, the equivalent capacitance should be

$$C=\frac{\varepsilon_0\varepsilon_r S}{d-nr} \tag{5}$$

From Eq. (5), we know that the capacitance increases with an increase of the number of metal plates. On the other hand, energy loss would occur in the metals as the electric field force does work on the free electrons by moving them in the metal plates under the low frequency alternative field (TENG working frequency). Therefore, the thickness of the plates should be reduced and leak current between nearby plates should be avoided.

If we insert m pieces of small plates in one layer and repeat the process for n layers, as shown in Fig. 5(b), the equivalent capacitance is

$$\begin{aligned} C&=\frac{\varepsilon_0\varepsilon_r mA}{d-nr}+\frac{\varepsilon_0\varepsilon_r (S-mA)}{d}\\ &=\frac{\varepsilon_0\varepsilon_r S}{d}+\varepsilon_0\varepsilon_r mA\left(\frac{1}{d-nr}-\frac{1}{d}\right)\end{aligned} \tag{6}$$

where, $A = l^2$ is the area of each metal plate. From Eq. (6), we can see that C increases with an increase of m and n. Similarly, to reduce the energy loss, the thickness of the metal plate should be small.

If we substitute the metal plates with numerous metal NPs (with diameter a) (Fig. 5(c)), the equivalent capacitance can still be calculated from Eq. (6), except that m and n are infinite and $r = a$, $A = \pi(a/2)^2$.

$$C=\frac{\varepsilon_0\varepsilon_r S}{d}+\varepsilon_0\varepsilon_r m\pi\left(a/2\right)^2\left(\frac{1}{d-na}-\frac{1}{d}\right) \tag{7}$$

The smaller particle size results in a larger number of micro-capacitors in the dielectric material. Consequently, filling conductive nanoparticles into a dielectric material can greatly enhance the capacitance of the capacitor; in other words, this approach can largely enhance energy storage in the capacitor.

The structure of the TENG based on the VMCs@PDMS film may classify it as a capacitor, as shown in Fig. 6(a1), given that the negative charges accumulate on the

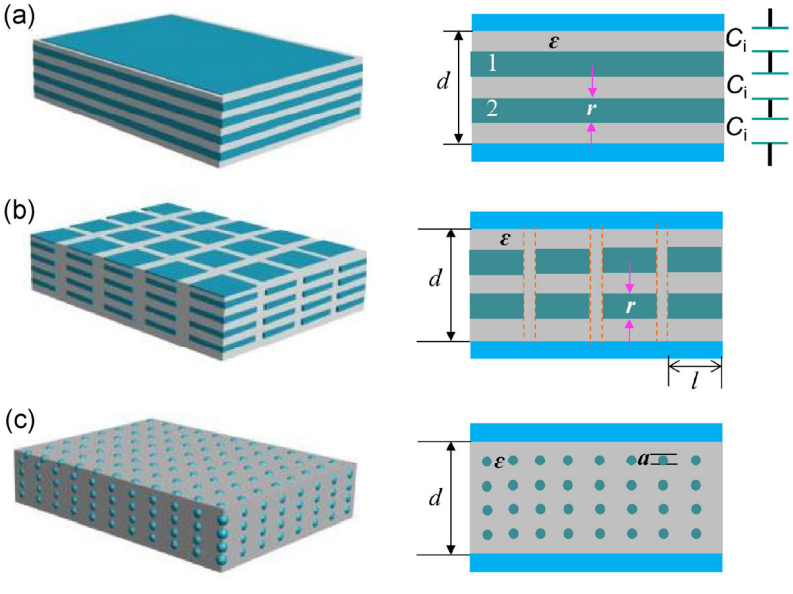

Figure 5 Schematic diagram of the capacitor structure with different shapes and sizes of metal materials filled in PDMS. (a) Larger metal sheets with thickness r and area S as the electrodes, and the equivalent capacitance structure, (b) smaller metal square sheets with thickness r and side length l, (c) numerous metal NPs with diameter a in PDMS.

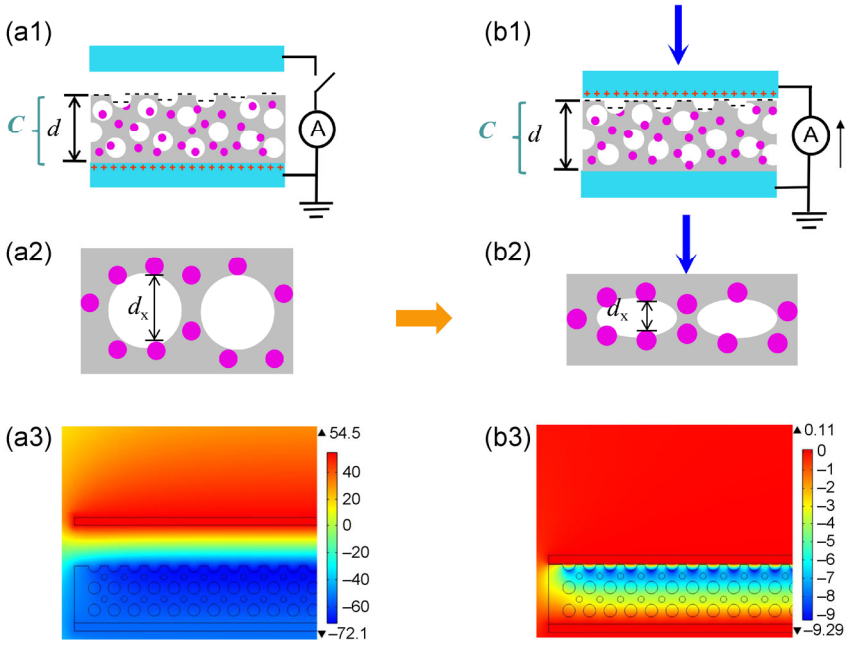

Figure 6 Schematic diagram of TENG based on VMCs@PDMS film illustrating enhanced electric output. (a1) Negative charges on surface of exposed PDMS and positive charges induced on bottom electrode when top electrode does not make contact with bottom electrode, (a2) enlarged region of VMCs@PDMS film indicating the micro-capacitors present in it, and (a3) the potential distribution calculated by COMSOL. Current flowing (b1) when the upper electrode connects with the bottom electrode. (b2) Capacitance of micro-capacitor increases as d_x decreases under applied compression and (b3) potential distribution calculated by COMSOL.

exposed surface of PDMS and positive charges are induced on the bottom electrode when the top electrode does not make contact with the bottom electrode. Therefore, the capacitance C determines the surface tribo-charges on PDMS. When the upper electrode connects with or separates from the bottom electrode, a current alternately flows between the electrodes through an external circuit (Fig. 6(b1)). During this process, the maximum current that can be obtained depends on the maximum charge accumulated on the surface of PDMS. To assess how the pores affect the capacitance of the TENG, we enlarged a part of the film (Fig. 6(a2)). The distance d_x between two Ag particles becomes variable in the presence of pores. The value of d_x decreases when an applied force presses the film, which increases the capacitance of the micro-capacitor formed by two Ag particles (Fig. 6(b2)). However, if d_x is too small, tunnel current would be produced between the two particles, which accounts for the decrease of the output current when the applied force exceeds F_0. COMSOL was employed to evaluate the enhanced capacitance of the VMCs@PDMS film. The potential distributions are shown in Figs. 6(a3) and 6(b3) under separation and contact processes, respectively.

4 Conclusion

In summary, VMCs were embedded in PDMS by filling PDMS with silver NPs and forming a cellular structure in PDMS. The electric output of the TENG based on the VMCs@PDMS films was systematically investigated with variation of the filling content of silver NPs and the pore ratio and size. The relative permittivity, dielectric loss, and capacitance of the VMCs@PDMS films were characterized. Theoretical analysis was used to explain the enhanced output power of the TENG based on the VMCs@PDMS film. The obvious advantages of the VMCs@PDMS film are as follows: (1) the enhanced surface charge accumulation on PDMS due to the enhanced effective capacitance derived from the micro-capacitors formed from the Ag NPs; (2) the enlarged friction area generated by forming pores in PDMS; (3) the controlled electrical output in response to an applied force on the TENG based on the VMCs@PDMS film due to the

variable micro-capacitors. The output current of the TENG based on the VMCs@PDMS film is 4 times higher than that of the TENG based on the pure PDMS film, and the output power density reached 6 $W \cdot m^{-2}$ at the load resistance of 20 MΩ; the device could be used to light about one hundred LEDs in series with good stability. This study sheds light on the physical nature of conductive nanoparticle fillings and cellular structures in dielectric polymers.

Acknowledgements

This work is supported by National Natural Science Foundation of China (Nos. 51572040 and 51402112), Chongqing University Postgraduates' Innovation Project (No. CYS15016), the National High-tech R&D Program of China (No. 2015AA034801), the Fundamental Research Funds for the Central Universities (Nos. CQDXWL-2014-001 and CQDXWL-2013-012).

Electronic Supplementary Material: Supplementary material (Fig. S1 shows the SEM image of silver NPs, sugar particles and XRD patterns of different PDMS composite film, respectively; Fig. S2 shows the SEM image of different PDMS film; Fig. S3 shows the output current density and voltage of the TENG based on MCs@PDMS film; Fig. S4 shows the current signals of the TENG based on VMCs@PDMS film and the digital images of different sizes of filling sugar particles; Fig. S5 shows the output open-circuit voltage under the variable relative humidity; Table S1 shows the dielectric characteristic of the MCs@PDMS films and VMCs@PDMS films, respectively with various Ag NPs contents and porosity ratios) is available in the online version of this article at http://dx.doi.org/10.1007/s12274-016-1294-4.

References

[1] Wang, S. H.; Lin, L.; Wang, Z. L. Nanoscale triboelectric-effect-enabled energy conversion for sustainably powering portable electronics. *Nano Lett.* **2012**, *12*, 6339–6346.

[2] Zhu, G.; Pan, C. F.; Guo, W. X.; Chen, C. Y.; Zhou, Y. S.; Yu, R. M.; Wang, Z. L. Triboelectric-generator-driven pulse electrodeposition for micropatterning. *Nano Lett.* **2012**, *12*, 4960–4965.

[3] Zhu, G.; Lin, Z. H.; Jing, Q. S.; Bai, P.; Pan, C. F.; Yang, Y.; Zhou, Y. S.; Wang, Z. L. Toward large-scale energy harvesting by a nanoparticle-enhanced triboelectric nanogenerator. *Nano Lett.* **2013**, *13*, 847–853.

[4] Tang, W.; Han, C. B.; Zhang, C.; Wang, Z. L. Cover-sheet-based nanogenerator for charging mobile electronics using low-frequency body motion/vibration. *Nano Energy* **2014**, *9*, 121–127.

[5] Fan, F. R.; Tian, Z. Q.; Wang, Z. L. Flexible triboelectric generator. *Nano Energy* **2012**, *1*, 328–334.

[6] Zhu, G.; Wang, A. C.; Liu, Y.; Zhou, Y. S.; Wang, Z. L. Functional electrical stimulation by nanogenerator with 58 V output voltage. *Nano Lett.* **2012**, *12*, 3086–3090.

[7] Chen, S. W.; Gao, C. Z.; Tang, W.; Zhu, H. R.; Han, Y.; Jiang, Q. W.; Li, T.; Cao, X.; Wang, Z. L. Self-powered cleaning of air pollution by wind driven triboelectric nanogenerator. *Nano Energy* **2015**, *14*, 217–225.

[8] Bae, J.; Lee, J.; Kim, S.; Ha, J.; Lee, B. S.; Park, Y.; Choong, C.; Kim, J. B.; Wang, Z. L.; Kim, H. Y. et al. Flutter-driven triboelectrification for harvesting wind energy. *Nat. Commun.* **2014**, *5*, 4929.

[9] Wen, Z.; Chen, J.; Yeh, M. H.; Guo, H. Y.; Li, Z. L.; Fan, X.; Zhang, T. J.; Zhu, L. P.; Wang, Z. L. Blow-driven triboelectric nanogenerator as an active alcohol breath analyzer. *Nano Energy* **2015**, *16*, 38–46.

[10] Zhang, L.; Zhang, B. B.; Chen, J.; Jin, L.; Deng, W. L.; Tang, J. F.; Zhang, H. T.; Pan, H.; Zhu, M. H.; Yang, W. Q. et al. Lawn structured triboelectric nanogenerators for scavenging sweeping wind energy on rooftops. *Adv. Mater.* **2016**, *28*, 1650–1656.

[11] Wang, X. F.; Niu, S. M.; Yin, Y. J.; Yi, F.; You, Z.; Wang, Z. L. Triboelectric nanogenerator based on fully enclosed rolling spherical structure for harvesting low-frequency water wave energy. *Adv. Energy Mater.* **2015**, *5*, 1501467.

[12] Jiang, T.; Zhang, L. M.; Chen, X. Y.; Han, C. B.; Tang, W.; Zhang, C.; Xu, L.; Wang, Z. L. Structural optimization of triboelectric nanogenerator for harvesting water wave energy. *ACS Nano* **2015**, *9*, 12562–12572.

[13] Choi, D.; Lee, S.; Park, S. M.; Cho, H.; Hwang, W.; Kim, D. S. Energy harvesting model of moving water inside a tubular system and its application of a stick-type compact triboelectric nanogenerator. *Nano Res.* **2015**, *8*, 2481–2491.

[14] Lin, Z. H.; Cheng, G.; Lee, S.; Pradel, K. C.; Wang, Z. L. Harvesting water drop energy by a sequential contact-electrification and electrostatic-induction process. *Adv. Mater.* **2014**, *26*, 4690–4696.

[15] Chen, J.; Yang, J.; Li, Z. L.; Fan, X.; Zi, Y. L.; Jing, Q. S.; Guo, H. Y.; Wen, Z.; Pradel, K. C.; Niu, S. M. et al. Networks of triboelectric nanogenerators for harvesting water wave

energy: A potential approach toward blue energy. *ACS Nano* **2015**, *9*, 3324–3331.

[16] Su, Y. J.; Wen, X. N.; Zhu, G.; Yang, J.; Chen, J.; Bai, P.; Wu, Z. M.; Jiang, Y. D.; Wang, Z. L. Hybrid triboelectric nanogenerator for harvesting water wave energy and as a self-powered distress signal emitter. *Nano Energy* **2014**, *9*, 186–195.

[17] Yang, J.; Chen, J.; Liu, Y.; Yang, W. Q.; Su, Y. J.; Wang, Z. L. Triboelectrification-based organic film nanogenerator for acoustic energy harvesting and self-powered active acoustic sensing. *ACS Nano* **2014**, *8*, 2649–2657.

[18] Yu, A. F.; Song, M.; Zhang, Y.; Zhang, Y.; Chen, L. B.; Zhai, J. Y.; Wang, Z. L. Self-powered acoustic source locator in underwater environment based on organic film triboelectric nanogenerator. *Nano Res.* **2015**, *8*, 765–773.

[19] Zhao, T.; Zhang, C.; Han, C. B.; Fan, F. R.; Tang, W.; Wang, Z. L. Woven structured triboelectric nanogenerator for wearable devices. *ACS Appl. Mater. Interfaces* **2014**, *6*, 14695−14701.

[20] Zhong, Q. Z.; Zhong, J. W.; Cheng, X. F.; Yao, X.; Wang, B.; Li, W. B.; Wu, N.; Liu, K.; Hu, B.; Zhou, J. Paper-based active tactile sensor array. *Adv. Mater.* **2015**, *27*, 7130−7136.

[21] Wu, Y. C.; Zhong, X. D.; Wang, X.; Yang, Y.; Wang, Z. L. Hybrid energy cell for simultaneously harvesting wind, solar, and chemical energies. *Nano Res.* **2014**, *7*, 1631–1639.

[22] Xia, X. N.; Liu, G. L.; Guo, H. Y.; Leng, Q.; Hu, C. G.; Xi, Y. Honeycomb-like three electrodes based triboelectric generator for harvesting energy in full space and as a self-powered vibration alertor. *Nano Energy* **2015**, *15*, 766–775.

[23] Xia, X. N.; Liu, G. L.; Chen, L.; Li, W. L.; Xi, Y.; Shi, H. F.; Hu, C. G. Foldable and portable triboelectric-electromagnetic generator for scavenging motion energy and as a sensitive gas flow sensor for detecting breath personality. *Nanotechnology* **2015**, *26*, 475402.

[24] Niu, S. M.; Wang, X. F.; Yi, F.; Zhou, Y. S.; Wang, Z. L. A universal self-charging system driven by random biomechanical energy for sustainable operation of mobile electronics. *Nat. Commun.* **2015**, *6*, 8975.

[25] Cheng, G.; Lin, Z. H.; Du, Z. L.; Wang, Z. L. Simultaneously harvesting electrostatic and mechanical energies from flowing water by a hybridized triboelectric nanogenerator. *ACS Nano* **2014**, *8*, 1932–1939.

[26] Wang, B.; Zhong, J. W.; Zhong, Q. Z.; Wu, N.; Cheng, X. F.; Li, W. B.; Liu, K.; Hu, B.; Zhou, J. Sandwiched composite fluorocarbon film for flexible electret generator. *Adv. Electron. Mater*. **2016**, *2*, 1500408.

[27] Wu, N.; Cheng, X. F.; Zhong, Q. Z.; Zhong, J. W.; Li, W. B.; Wang, B.; Hu, B.; Zhou, J. Cellular polypropylene piezoelectret for human body energy harvesting and health monitoring. *Adv. Funct. Mater.* **2015**, *25*, 4788–4794.

[28] Chen, J.; Guo, H. Y.; He, X. M.; Liu, G. L.; Xi, Y.; Shi, H. F.; Hu, C. G. Enhancing performance of triboelectric nanogenerator by filling high dielectric nanoparticles into sponge PDMS film. *ACS Appl. Mater. Interfaces* **2016**, *8*, 736–744.

[29] He, X. M.; Guo, H. Y.; Yue, X. L.; Gao, J.; Xi, Y.; Hu, C. G. Improving energy conversion efficiency for triboelectric nanogenerator with capacitor structure by maximizing surface charge density. *Nanoscale* **2015**, *7*, 1896–1903.

[30] Wang, S. H.; Xie, Y. N.; Niu, S. M.; Lin, L.; Liu, C.; Zhou, Y. S.; Wang, Z. L. Maximum surface charge density for triboelectric nanogenerators achieved by ionized-air injection: Methodology and theoretical understanding. *Adv. Mater.* **2014**, *26*, 6720–6728.

[31] Lee, K. Y.; Chun, J.; Lee, J.-H.; Kim, K. N.; Kang, N.-R.; Kim, J.-Y.; Kim, M. H.; Shin, K.-S; Gupta, M. K.; Baik, J. M. et al. Hydrophobic sponge structure-based triboelectric nanogenerator. *Adv. Mater.* **2014**, *26*, 5037–5042.

[32] Kim, D.; Park, S. J.; Jeon, S. B.; Seol, M. L.; Chhoi, Y. K. A triboelectric sponge fabricated from a cube sugar template by 3D soft lithography for superhydrophobicity and elasticity. *Adv. Electron. Mater.* **2016**, *2*, 1500331.

[33] Jeong, C. K.; Baek, K. M.; Niu, S. M.; Nam, T. W.; Hur, Y. H.; Park, D. Y.; Hwang, G.-T; Byun, M.; Wang, Z. L.; Jung, Y. S. et al. Topographically-designed triboelectric nanogenerator via block copolymer self-assembly. *Nano Lett.* **2014**, *14*, 7031–7038.

[34] Chun, J. S.; Kim, J. W.; Jung, W. S.; Kang, C. Y.; Kim, S. W.; Wang, Z. L.; Baik, J. M. Mesoporous pores impregnated with Au nanoparticles as effective dielectrics for enhancing triboelectric nanogenerator performance in harsh environments. *Energy Environ. Sci.* **2015**, *8*, 3006–3012.

[35] Li, W. B.; Wu, N.; Zhong, J. W.; Zhong, Q. Z.; Zhao, S.; Wang, B.; Cheng, X. F.; Li, S. L.; Liu, K.; Hu, B. et al. Theoretical study of cellular piezoelectret generators. *Adv. Funct. Mater.* **2016**, *26*, 1964–1974.

[36] Xie, Y. N.; Wang, S. H.; Lin, L.; Jing, Q. S.; Lin, Z. H.; Niu, S. M.; Wu, Z. Y.; Wang, Z. L. Rotary triboelectric nanogenerator based on a hybridized mechanism for harvesting wind energy. *ACS Nano* **2013**, *7*, 7119–7125.

[37] Ko, Y. H.; Nagaraju, G. L.; Lee, S. H.; Yu, J. S. PDMS-based triboelectric and transparent nanogenerators with ZnO nanorod arrays. *ACS Appl. Mater. Interfaces* **2014**, *6*, 6631–6637.

[38] Chen, J.; Zhu, G.; Yang, W. Q.; Jing, Q. S.; Bai, P.; Yang, Y.; Hou, T. C.; Wang, Z. L. Harmonic-resonator-based triboelectric nanogenerator as a sustainable power source and a self-powered active vibration sensor. *Adv. Mater.* **2013**, *25*, 6094–6099.